Data-driven enhancement of fracture paths in random composites

Johann Guilleminot [a,*], John E. Dolbow [b]

[a] *Department of Civil and Environmental Engineering, Duke University, Durham, NC 27708, USA*
[b] *Department of Mechanical Engineering and Materials Science, Duke University, Durham, NC 27708, USA*

ARTICLE INFO

ABSTRACT

A data-driven framework for the enhancement of fracture paths in random heterogeneous microstructures is presented. The approach relies on the combination of manifold learning, introduced to explore the geometrical structure exhibited by crack patterns and achieve efficient dimensionality reduction, and *a posteriori* crack path reconstruction, defined through a Markovianization. The proposed methodology enables the generation of new crack patterns, the underlying structure and dynamical properties of which are consistent, by construction, with those obtained from high-fidelity computations. These sampled cracks can subsequently be used to enrich datasets and perform uncertainty quantification at multiple scales, at a fraction of the computational cost associated with full-scale simulations. A numerical example where the initial dataset is obtained from a recently developed gradient damage formulation is provided to demonstrate the effectiveness of the method. While the methodology is presently applied to digital data, it can also be deployed on experimental measurements.

1. Introduction

Put forward by the growth of both available data and computing resources, Machine Learning (ML) techniques (and within that family, Deep Learning (DL) approaches in particular) have recently resurged as very promising tools capable of accommodating high-dimensional inputs and highly nonlinear mappings. In this context, there has been a proliferation of works involving ingredients of ML for computational physics. Examples include, *in a non-exhaustive manner*, material constitutive modeling [1–11], discovery of partial and ordinary differential equations [12,13], inverse problem solving (see, e.g., [14–18]), random microstructure modeling and reconstruction [19,20], and uncertainty propagation [21,22]. Uncertainty quantification frameworks for DL were also proposed in [23,24]. Restricting the attention to surrogate modeling for fracture, Neural Networks (NN) were used, for instance, in [25] to predict the growth and coalescence of (preexisting) cracks in a geologic material; see [26,27] for various extensions including different types of NN and reduced order modeling. Convolutional neural networks were considered in [28] to predict crack profiles in a polycrystalline alloy, based on microstructural data.

While encouraging, the use of deep learning methods in computational mechanics also raises a series of well-known issues, among which the design of optimal architectures and the integration of constraints inferred from physics [2,29,30]. Conceptually, the application of DL for crack path prediction amounts to defining a sequence of local approximations, corresponding to the time discretization of the fracture process. For microstructure-sensitive crack paths, this necessitates tracking a large number of input variables, some of which may not be active near the crack tip at a given time instance.

The main objective pursued in this paper is to propose an approach enabling the enrichment of datasets, obtained either through computational simulations or by means of physical experiments. While this may possibly be achieved by using Generative Adversarial Networks (GANs), we aim to develop a methodology that leverages the "regularity" induced by the properties of the microstructural fields, which are often assumed to be homogeneous (meaning that the systems of marginal laws defining these random fields are invariant under translations in space) and isotropic (that is, the systems of marginal laws are also invariant under rotations) [31,32]. These two properties manifest themselves through a "geometrical signature" defining a manifold over the entire crack path, suggesting that crack paths could be described, under the above assumptions, in a low dimensional space. Motivated by these remarks, we propose a sampling-based approach taking advantage of the aforementioned invariance properties. The approach relies on the combination of manifold learning, which is introduced to reveal the geometrical structure of crack patterns and used as a means to achieve dimensionality reduction, and *a posteriori* Markov-type point selection, which is necessary to reconstruct crack profiles from newly synthesized, unlabeled data.

* Corresponding author.
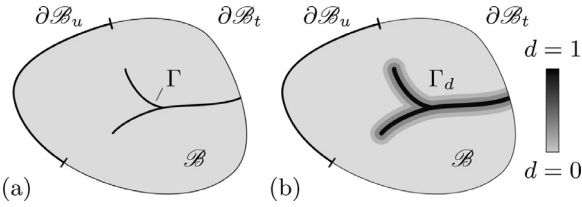 *E-mail address:* johann.guilleminot@duke.edu (J. Guilleminot).

Fig. 1. (a) Sketch of a body, $\mathscr{B}$, with an internal discontinuity Γ. (b) A regularized representation of the internal discontinuity. Constitutive phases are not represented for the sake of readability.

This paper is organized as follows. The high-fidelity formulation used to generate the reference dataset is first presented in Section 2. The machine learning framework and selection procedure are then introduced in Section 3. Results are presented all along the paper to illustrate the methodological steps.

2. High-fidelity model for crack propagation

2.1. Phase-field/gradient damage formulation

We consider an arbitrary, heterogeneous body $\mathscr{B} \subset \mathbb{R}^n$ (with $n \in \{1, 2, 3\}$) with external boundary $\partial\mathscr{B}$ with $\partial\mathscr{B}_t \cap \partial\mathscr{B}_u = \emptyset$, $\partial\mathscr{B}_t \cup \partial\mathscr{B}_u = \partial\mathscr{B}$ and an internal crack surface Γ as shown in Fig. 1a. Without loss of generality, we consider a two-phase composite system, and denote with the subscripts i and m the inclusion and matrix phases, respectively. The state of the system is described by two independent variables, the vector displacement field $\mathbf{u}$ and a scalar damage field d.

We follow the approach described in [33] wherein the damage plays the role of approximating the crack surface Γ by its regularized counterpart Γ_d as shown in Fig. 1b. Following conventions, the damage takes values in [0,1], with $d = 0$ away from the crack surface and $d = 1$ in the vicinity of the crack. Small deformations and deformation gradients are assumed. The infinitesimal strain tensor $\boldsymbol{\varepsilon}$ is defined as $\boldsymbol{\varepsilon} = \frac{1}{2}(\nabla\mathbf{u} + (\nabla\mathbf{u})^T)$. We assume that the damage field acts only to degrade the tensile resistance of the body and that crack propagation is prohibited under compression. Following [34], this is effected by employing a spectral decomposition of $\boldsymbol{\varepsilon}$ into positive and negative components, via $\boldsymbol{\varepsilon}_{\pm} := \sum_{a=1}^{n} \langle \varepsilon_a \rangle_{\pm} \mathbf{n}_a \otimes \mathbf{n}_a$, where $\{\varepsilon_a\}_{a=1\ldots n}$ are the principal strains and $\{\mathbf{n}_a\}_{a=1\ldots n}$ the principal strain directions. The positive and negative operators $\langle \cdot \rangle_+$ and $\langle \cdot \rangle_-$ are given by

$$\langle x \rangle_+ = \begin{cases} x & \text{if } x \geq 0, \\ 0 & \text{otherwise}, \end{cases} \quad \text{and} \quad \langle x \rangle_- = \begin{cases} x & \text{if } x \leq 0, \\ 0 & \text{otherwise}. \end{cases}$$

The decomposition of the strain makes it possible to define tensile and compressive elastic strain energy densities. We restrict attention to isotropic linear elasticity, and define these strain energy densities by $\psi_0^+(\boldsymbol{\varepsilon}) = \frac{1}{2}\lambda_s\langle\mathrm{Tr}\boldsymbol{\varepsilon}\rangle_+^2 + \mu_s\boldsymbol{\varepsilon}_+ : \boldsymbol{\varepsilon}_+$ and $\psi_0^-(\boldsymbol{\varepsilon}) = \frac{1}{2}\lambda_s\langle\mathrm{Tr}\boldsymbol{\varepsilon}\rangle_-^2 + \mu_s\boldsymbol{\varepsilon}_- : \boldsymbol{\varepsilon}_-$, where $\lambda_s > 0$ and $\mu_s > 0$ are the Lamé coefficients in the constitutive phase $s \in \{i, m\}$. The stress $\boldsymbol{\sigma}$ is assumed to decay with the damage according to $\boldsymbol{\sigma}(d) = g(d)\frac{\partial\psi_0^+}{\partial\boldsymbol{\varepsilon}} + \frac{\partial\psi_0^-}{\partial\boldsymbol{\varepsilon}}$, where g is a degradation function. In this work, we use the degradation function proposed by Lorentz [35]:

$$g(d) = \frac{(1-d)^2}{(1-d)^2 + \frac{M}{\psi_c}d(1+d)},$$

where M is a mobility constant such that $M = 3\mathscr{G}_c/(8\ell)$, where $\mathscr{G}_c$ is the critical energy release rate and ℓ denotes the regularization length, and ψ_c is a threshold energy for damage initiation defined as $\psi_c = \sigma_c^2/(2E)$, with E the Young's modulus. Note that phase-specific subscripts are not used in these material parameters to
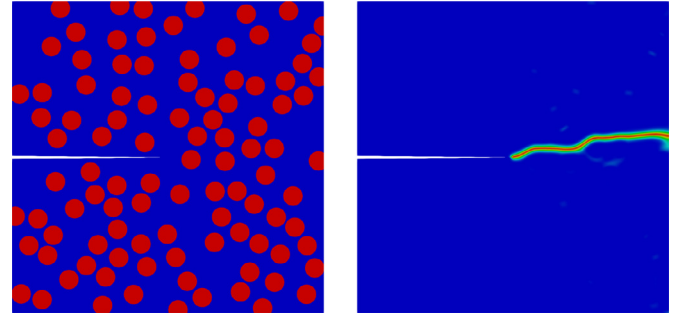

Fig. 2. One microstructural sample and associated crack path for mode I fracture.

simplify notation. In this work, we take $\ell = E\mathscr{G}_c/(4\sigma_c^2)$ (see Section 2.3 in [33]).

In the present work, we confine attention to quasi-static loadings where inertial effects can be neglected. The governing equations are then given by the macro-scale force balance and the micro-force balance, and read

$$\mathrm{Div}\boldsymbol{\sigma} = 0 \qquad \text{on } \mathscr{B} \times]0, T[\tag{1}$$

$$2\ell^2\Delta d - \frac{g'(d)}{M}\psi_0^+ = 1 \qquad \text{on } \mathscr{B} \times]0, T[\tag{2}$$

subject to the boundary conditions $\mathbf{u} = \bar{\mathbf{u}}$ on $\partial\mathscr{B}_u \times]0, T[$, $\boldsymbol{\sigma} \cdot \mathbf{n} = \bar{\mathbf{t}}$ on $\partial\mathscr{B}_t \times]0, T[$, and $\nabla d \cdot \mathbf{n} = 0$ on $\partial\mathscr{B} \times]0, T[$, and subject to the constraint $\dot{d} \geq 0$ on $\mathscr{B} \times]0, T[$ (enforced using an augmented Lagrange method). The above governing equations and boundary conditions are re-cast in an equivalent variational form, and then finite-element approximations are constructed for the displacement and damage fields (see [33] for details of the implementation).

2.2. Numerical result on a microstructural sample

The formulation detailed in Section 2.1 is now applied to a monodisperse random medium exhibiting statistical isotropy. This prototypical microstructure is relevant to a wide variety of materials, ranging from concrete to cross-sectional models of fiber-matrix composites. Moreover, it presents a high level of stochasticity in terms of crack paths due to limited localization (see, e.g., [36]). In this work, microstructural samples are obtained by using the molecular-dynamics-based algorithm detailed in [37]. Material parameters for the matrix are set to: $\lambda_m = 121$ GPa, $\mu_m = 80.77$ GPa, $(\mathscr{G}_c)_m = 2.7$ N/mm and $(\sigma_c)_m = 2.0$ GPa. A contrast of 10 is introduced between the properties of the matrix phase and those associated with the inclusions (e.g., $\lambda_i/\lambda_m = 10$). A crack path associated with one sample of the microstructure and mode I fracture is shown in Fig. 2. While the cracks were not a-priori restricted to propagate only in the matrix, all simulation results exhibited this form of crack growth. This is consistent with common observations of simulated crack trajectories in composites with relatively stiff inclusions.

3. Hybrid unsupervised-supervised approach

Within the framework introduced in Section 2, diffuse crack paths can be interpreted as realizations of a space-time random field $\{d(\mathbf{x}, t), \mathbf{x} \in \Omega, t \in [0, T]\}$, defined on a given probability space $(\Theta, \mathscr{T}, P)$ and with values in [0,1], with $0 \leqslant T < +\infty$. Without loss of generality, we assume in what follows that crack path variability is generated by microstructural randomness. Boundary conditions are fixed throughout this section.
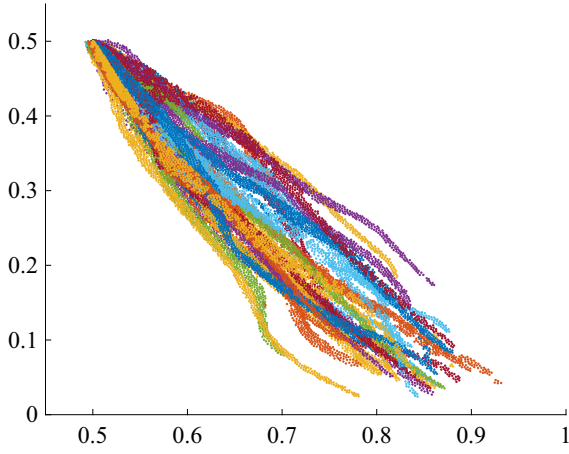
Fig. 3. Discretized representations of crack patterns obtained from phase-field simulations with $N = 45$ independent microstructures (mode II). Each color is associated with one microstructural sample.
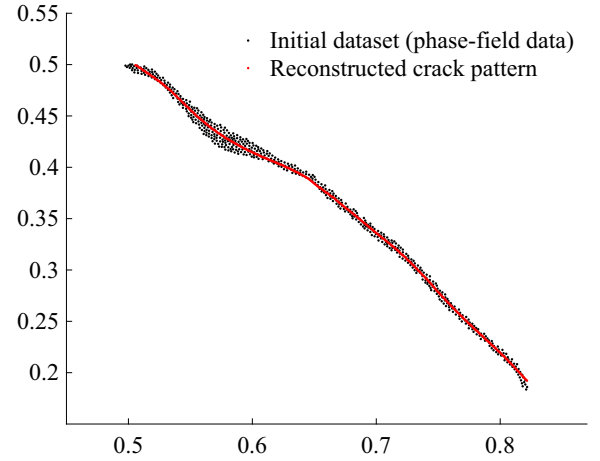

Fig. 4. Filtered crack pattern for microstructure #3.

Fig. 5. Filtered crack patterns, obtained by postprocessing the phase-field dataset shown in Fig. 3.

3.1. Manifold learning formulation

3.1.1. Data filtering

The first step of the approach consists in computing "filtered" (that is, non-diffuse) crack patterns that will be used as training points within the unsupervised learning component of the methodology and to evaluate conditional probabilities for pattern reconstruction. To that end, let $\mathscr{I}_d$ be the damage indicator function such that $\mathscr{I}_d(\boldsymbol{x}) = 1$ if $d(\boldsymbol{x}, T) > 0$ and $\mathscr{I}_d(\boldsymbol{x}) = 0$ otherwise, for all $\boldsymbol{x}$ in Ω (note that the time instance $t = T$ is considered here, so that the entire crack path is characterized). For a given sample θ_i of the random microstructure, let Ω_d^i denote the set of all (non-ordered) points in Ω where damage occurs, $\mathscr{I}_d(\boldsymbol{x}) = 1$ for all $\boldsymbol{x} \in \Omega_d^i$, and let $N_i = |\Omega_d^i|$. The set of raw simulated data, obtained from the gradient damage formulation, is then written as $\Omega_d = \bigcup_{i=1}^N \Omega_d^i$, where N denotes the number of microstructures sampled. Plots of all points belonging to Ω_d^i, $1 \leqslant i \leqslant N$, are shown in Fig. 3.

Various strategies were proposed to reconstruct crack patterns based on diffuse (phase-field) representations; see [38] for an optimization-based approach, for instance. In this work, a crack path is identified with the set of points that have the highest density of surrounding damage. In practice, the crack is localized by computing a scale-space representation of the damage indicator function, in which the scale level in the Gaussian kernel is deduced from a parametric analysis, and through ridge detection on the smooth function thus obtained. It should be noticed that while this choice may be critical in studies focused on the development of phase-field formulations, it is not expected to impact the presented methodology and results. The initial reference dataset and reconstructed crack for microstructure #3 (for which the band associated with the diffuse damage field has a location-dependent width) are shown in Fig. 4. The set of all reference crack paths, obtained by filtering the data in Fig. 3, is shown in Fig. 5.

3.1.2. Mathematical formulation in dimension 2

The data corresponding to N (filtered) crack paths are gathered in a $(2 \times N_D)$ matrix $[D] = [[D^{(1)}], \ldots, [D^{(N)}]]$, where $N_D = |\Omega_d| = \sum_{i=1}^N N_i$. The data points associated with the i-th crack path are written as $[D^{(i)}] = [\boldsymbol{d}^{i1}, \ldots, \boldsymbol{d}^{iN_i}]$, $1 \leqslant i \leqslant N$, and $\boldsymbol{d}^{ij}$ is the vector of coordinates of the j–th point in Ω_d^i. Following [39], $[D]$ is interpreted from now on as the realization of a random matrix $[\boldsymbol{D}]$ defined on $(\Theta, \mathscr{T}, P)$. The columns of $[D]$ correspond to independent samples of a random vector $\boldsymbol{D}$ defined by a probability measure
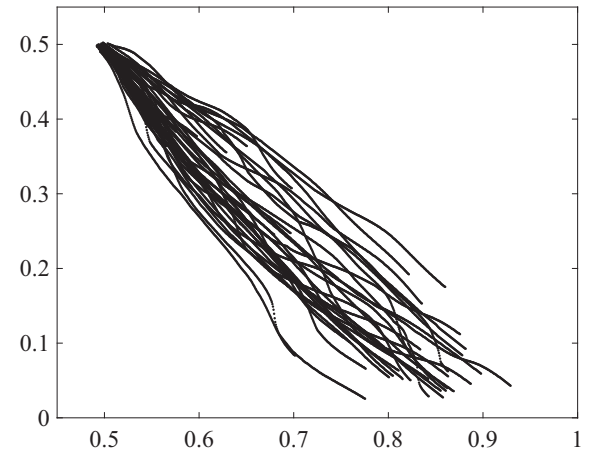
concentrated on the manifold that reflects microstructural details. It is common practice to normalize $[D]$ through a principal component analysis:

$$[D] = [\underline{D}] + [\Phi][\Lambda]^{1/2}[H], \qquad (3)$$

where $[\underline{D}] = [\underline{\boldsymbol{d}}, \ldots, \underline{\boldsymbol{d}}]$, with $\underline{\boldsymbol{d}} = \frac{1}{N_D} \sum_{i=1}^N \sum_{j=1}^{N_i} \boldsymbol{d}^{ij}$, $[\Lambda]$ and $[\Phi]$ are the matrices of eigenvalues and eigenvectors of the covariance matrix $[C] = \frac{1}{N_D} \sum_{i=1}^N \sum_{j=1}^{N_i} (\boldsymbol{d}^{ij} - \underline{\boldsymbol{d}})(\boldsymbol{d}^{ij} - \underline{\boldsymbol{d}})^{\mathsf{T}}$. The normalized dataset is thus given by

$$[H] = [\Lambda]^{-1/2}[\Phi]^{\mathsf{T}}([\underline{D}] - [D]), \qquad (4)$$

with $[H] = [\boldsymbol{h}^1, \ldots, \boldsymbol{h}^{N_D}]$, and $[H]$ can be seen as one realization of a normalized random matrix $[\boldsymbol{H}]$. The goal to enrich the dataset is then to draw new samples of $[\boldsymbol{H}]$ that can then be used to compute new samples of $[\boldsymbol{D}]$.

In order to ensure proper measure concentration, we follow the approach proposed in [39]. The strategy consists in using an Itô Stochastic Differential Equation (ISDE) to sample the probability measure estimated from the data, and in performing an appropriate change of measure in the ISDE through a diffusion map basis. Following the work of Coifman et al. [40], a direct effect of the projection is to concentrate the realizations on the manifold defined by the reference dataset. These ingredients are reviewed below.

The construction of the diffusion map basis proceeds as follows [40]. Let k_ϵ be the kernel defined as

$$k_\epsilon(\boldsymbol{h}, \boldsymbol{h}') = \exp(-\|\boldsymbol{h} - \boldsymbol{h}'\|/(4\epsilon)), \qquad (5)$$

where $\|\cdot\|$ denotes the Euclidean norm, and let $[K]$ be the symmetric matrix such that

$$K_{ij} = k_\epsilon(\boldsymbol{h}^i, \boldsymbol{h}^j), \quad 1 \leqslant i, j \leqslant N_D. \tag{6}$$

Let $[B]$ be the matrix with entries $B_{ij} = \delta_{ij} \sum_{k=1}^{N_D} [K]_{ik}$, and let $[P] = [B]^{-1}[K]$. Let $[P_S]$ be the matrix defined as $[P_S] = [B]^{1/2}[P][B]^{-1/2}$, and let $\{\lambda_i\}_{i=1}^{N_D}$ and $\{\boldsymbol{\phi}^{(i)}\}_{i=1}^{N_D}$ be the set of eigenvalues (ordered as a non-increasing sequence) and eigenvectors of $[P_S]$. A reduced-order representation is then obtained by retaining the m most significant eigenvalues and associated eigenvectors. The diffusion map basis is given as $[G] = [\boldsymbol{g}^{(1)}, \ldots, \boldsymbol{g}^{(m)}]$, where

$$\boldsymbol{g}^{(i)} = \lambda_i^S [B]^{-1/2} \boldsymbol{\phi}^{(i)}, \quad 1 \leqslant i \leqslant m, \tag{7}$$

and $S \in \mathbb{N}_*$ is a scale parameter related to the exploration of the underlying geometrical structure [40]. The reader is referred to [41] for discussions regarding the selection of hyperparameters. A reduced order representation of the random matrix $[\boldsymbol{H}]$ is finally defined as

$$[\boldsymbol{H}] = [\boldsymbol{Z}][G]^T, \tag{8}$$

where $[\boldsymbol{Z}]$ is a random matrix defined on $(\Theta, \mathscr{T}, P)$. The above relation can be inverted as $[\boldsymbol{Z}] = [\boldsymbol{H}][A]^T$, with $[A] = [G]([G]^T[G])^{-1}$.

The following ISDE was introduced in [39] to sample the reduced-order representation $[\boldsymbol{Z}]$: for $t \geqslant 0$,

$$\begin{cases} \mathrm{d}[\mathcal{Z}(t)] = [\mathcal{Y}(t)]\,\mathrm{d}t \\ \mathrm{d}[\mathcal{Y}(t)] = [\mathcal{L}([\mathcal{Z}(t)])]\,\mathrm{d}t - \gamma\,[\mathcal{Y}(t)]\,\mathrm{d}t + \sqrt{2\gamma}\,[\mathrm{d}\mathcal{W}(t)]' \end{cases}$$

with $[\mathcal{Z}(0)] = [H][A]$ and $[\mathcal{Y}(0)] = [\boldsymbol{N}][A]$ almost surely, where $[\boldsymbol{N}]$ is a $(2 \times N_D)$ random matrix whose columns are independent copies of the normalized Gaussian random vector in $\mathbb{R}^2$, and $\gamma > 0$ is a parameter. The matrix-valued function $[\mathcal{L}]$ is defined as

$$[\mathcal{L}([\mathcal{Z}(t)])] = [L([\mathcal{Z}(t)][G]^T)][A], \tag{9}$$

where

$$L([U])_{ij} = \frac{1}{f(\boldsymbol{u}^j)} \{\nabla_{\boldsymbol{u}^j} f(\boldsymbol{u}^j)\}_i \tag{10}$$

for any $(2 \times N_D)$ matrix $[U] = [\boldsymbol{u}^1, \ldots, \boldsymbol{u}^{N_D}]$, and f is the kernel density estimator constructed with the normalized data [42]. Finally, one has $[\mathrm{d}\mathcal{W}(t)] = [\mathrm{d}\boldsymbol{W}(t)][A]$, where $[\mathrm{d}\boldsymbol{W}(t)] = [\mathrm{d}\boldsymbol{W}^1(t), \ldots, \mathrm{d}\boldsymbol{W}^{N_D}(t)]$ and $\{\boldsymbol{W}^i\}_{i=1}^{N_D}$ are independent copies of the normalized Wiener process in $\mathbb{R}^2$. It can then be shown that $\lim_{t \to +\infty}[\mathcal{Z}(t)] = [\boldsymbol{Z}]$ in probability distribution, meaning that integrating the ISDE allows for the generation of samples of $[\boldsymbol{Z}]$ (and hence, of $[\boldsymbol{H}]$ and $[\boldsymbol{D}]$). When written in vector form, the above ISDE corresponds to the Langevin equation used in molecular dynamics simulations to model the effect of molecules outside the computational domain (the analogy being formally obtained by considering that all atoms have a mass equal to one, and a Langevin bath temperature set to $1/k_B$, with k_B the Boltzmann constant; γ is then called the collision frequency in the literature). In this context, many schemes were proposed to discretize the equation; see, e.g., [43] for details. In this work, the well-known Brünger–Brooks–Karplus (BBK) integrator is used [44].

3.1.3. Example: case of pure shear

We now apply the methodology to the dataset obtained for pure shear, shown in Fig. 5. In this case, $N_D = 19,880$ and the plot of the mapping $i \mapsto \lambda_i$ is shown in Fig. 6 for $1 \leqslant i \leqslant 1000$. Note that by construction, $\lambda_1 = 1$. Below, the order of truncation is determined by retaining all eigenvalues greater than 0.01, which yields $m = 166$. This underlines the substantial dimensionality reduction obtained through the manifold learning approach. New samples generated by integrating the ISDE are shown in Fig. 7 (100 additional samples of $[\boldsymbol{D}]$ are shown).
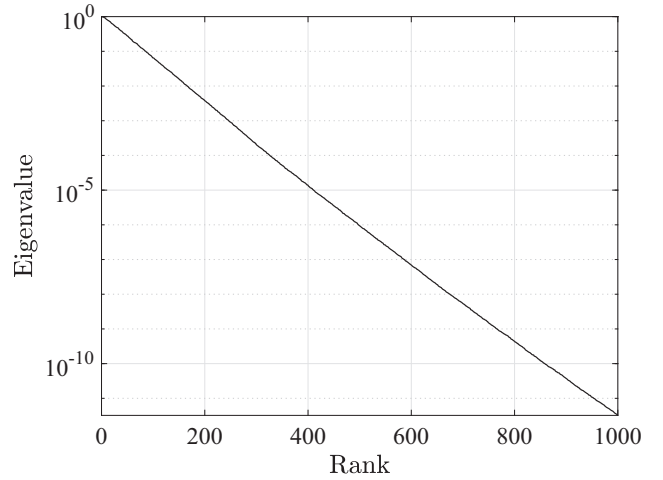

Fig. 6. Plot of $i \mapsto \lambda_i$ for $1 \leqslant i \leqslant 1000$.
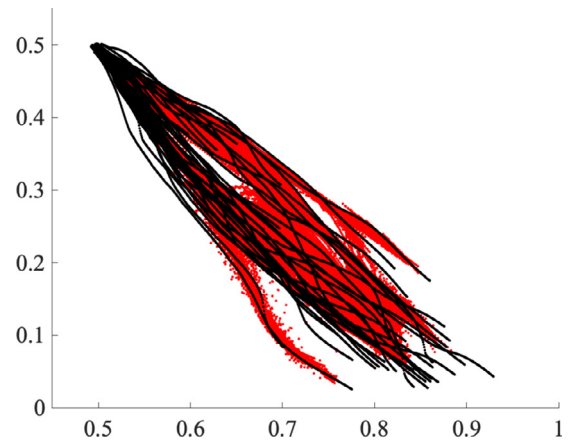

Fig. 7. New samples generated through probabilistic learning (red) and comparison with the reference dataset (black). (For interpretation of the references to color in this figure legend, the reader is referred to the web version of this article).

As expected, it is seen that the points generated through the reduced-order representation are well concentrated on the manifold induced from microstructural characteristics, thanks to the diffusion map basis. In the next section, a possible strategy to reconstruct crack is presented.

3.2. Crack path reconstruction

Let us consider the sequence $\{\boldsymbol{D}^k\}_{k \geqslant 1}$ of ordered points constituting a stochastic crack path (of arbitrary length). A natural way to describe the discretized crack is through a Markov chain (see, e.g., [45]). To that end, consider the representation $\{\boldsymbol{X}^k = (r_k, \alpha_k)\}_{k \geqslant 1}$ of the crack, where $r_{k+1} = \|\boldsymbol{D}^{k+1} - \boldsymbol{D}^k\|$ takes its values in $\mathscr{S}_r \subset \mathbb{R}_*^+$ and the angle α_k between successive segments takes its values in $\mathscr{S}_\alpha = [-\pi/2 + \epsilon_\alpha, \pi/2 - \epsilon_\alpha]$, with $0 < \epsilon_\alpha \ll 1$; see Fig. 8. For random composites that exhibit both stationarity and statistical isotropy, it is reasonable to assume homogeneity and finite memory, meaning that

$$P(\boldsymbol{X}^{k+1} \in B_{k+1} | \boldsymbol{X}^k \in B_k, \ldots, \boldsymbol{X}^1 \in B_1) \tag{11}$$

is equal to

$$P(\boldsymbol{X}^{k+1} \in B_{k+1} | \boldsymbol{X}^k \in B_k, \ldots, \boldsymbol{X}^{k-\nu+1} \in B_{k-\nu+1}) \tag{12}$$

for some positive integer ν and $\forall k \geqslant \nu$. The chain $\{\boldsymbol{Y}^k\}_k$, with $\boldsymbol{Y}^k = (\boldsymbol{X}^k, \ldots, \boldsymbol{X}^{k-\nu+1})$, then satisfies the Markov property. The choice of ν is application-dependent. While longer memory is expected
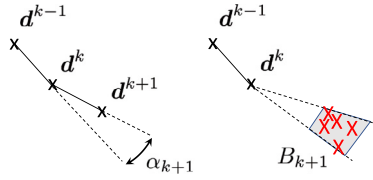
Fig. 8. Crack parameterization (left) and view of possible points (in red) identified through conditional probabilities (right). (For interpretation of the references to color in this figure legend, the reader is referred to the web version of this article).
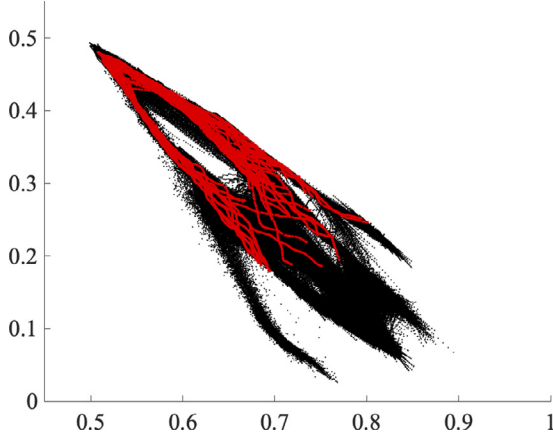

Fig. 10. New crack patterns (red) and reference dataset (black). (For interpretation of the references to color in this figure legend, the reader is referred to the web version of this article).

Fig. 9. Points (red) selected on the new dataset generated by the probabilistic learning approach (black). (For interpretation of the references to color in this figure legend, the reader is referred to the web version of this article).

to improve predictions, at least for $\nu \leqslant \nu^*$ (where ν^* is unknown *a priori*), it significantly increases the size of the Markovianization. This increase requires using larger training datasets and may complicate data processing over multi-states. The memoryless case $\nu = 1$ is considered below, for the sake of illustration.

The reconstruction procedure consists in sampling the conditional distribution and in randomly selecting a point among all candidates in B_{k+1} (see the right panel in Fig. 8). The measure $|B_{k+1}|$ is assumed sufficiently small, so that the number of admissible candidates remains small and the random selection induces a negligible bias. Given the purpose of the study, stochastic jumps are not modeled, so that conditional probabilities can be evaluated for sets of the form

$$\mathscr{B}_k = [\underline{r} - \Delta r/2, \underline{r} + \Delta r/2] \times [\underline{\alpha}_k - \Delta\alpha/2, \underline{\alpha}_k + \Delta\alpha/2], \qquad (13)$$

where $\underline{r}$ is the mean of r_k, estimated from the dataset, $\Delta r > 0$ is a small parameter that has to be tuned using the training data (using, e.g., quantiles), $\underline{\alpha}_k$ is given by

$$\underline{\alpha}_k = -\frac{\pi}{2} + \epsilon_\alpha + (2k+1)\frac{\Delta\alpha}{2} \qquad (14)$$

and $\Delta\alpha$ is such that $|\mathscr{S}_\alpha| = \pi - 2\epsilon = N_\alpha \Delta\alpha$, with N_α an even integer (the value $N_\alpha = 46$ is selected below). When no points can be found in B_{k+1}, resampling is undertaken by increasing the measure along the radius of search until admissible candidates are found.

Examples of selected points are shown in Fig. 9, where the points generated by using the probabilistic learning approach are also displayed. Note that the selection was stopped after a fixed number of iterations in the presented results, which explains why the entire dataset was not fully explored. Depending on the application, a probabilistic stopping criterion based on e.g., crack length, can easily be implemented.

The new crack profiles obtained through the hybrid, data-driven approach can be compared with the training data in Fig. 10. By construction, these sampled crack paths exhibit two important properties inherited from the high-fidelity model, that are: (1) The
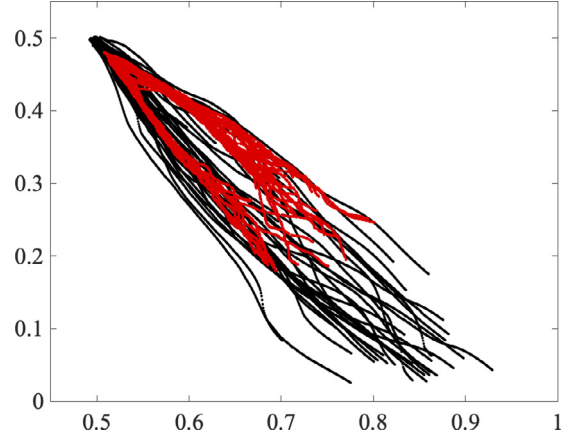
geometrical structure, as induced by fine-scale details; and (2) spatial evolution, as described by the matrix of transition probabilities. Note that the latter can be strongly affected by the value of ν (which defines the memory in the chain), which has to be carefully chosen based on the application.

3.3. Remarks

The proposed methodology can accommodate other types of boundary conditions. Numerical results (which are not reported for the sake of brevity) were obtained for various settings balancing between mode I and mode II fracture, and the approach performed equally well in all cases. By construction, the approach can also handle the case of more complex loading paths where different modes arise as a function of time, provided that the training set remains informative about data concentration.

While the additional fracture paths are not associated with specific microstructural samples, macroscopic results can still be obtained by considering a background media characterized by homogenized elastic properties, defined under suitable boundary conditions (see, e.g., [46,47]).

Whereas none of the reference simulations (detailed in Section 2) exhibited crack branching, the latter could be described by splitting the selection procedure (once branching has occurred) and by properly adapting the sets of initial conditions for the Markovianizations.

4. Conclusion

In this paper, a hybrid, data-driven framework for the enrichment of fracture paths in random microstructures has been presented. Building upon standard assumptions associated with the stochastic representation of random media, the approach aims to take advantage of crack path regularity to achieve dimensionality reduction and enable statistical sampling. The strategy specifically relies on the combination of manifold learning, introduced to explore the geometrical structure exhibited by crack patterns, and *a posteriori* crack path reconstruction, defined through a Markovianization. A numerical example where the initial dataset was obtained from a phase-field/gradient damage formulation was provided to illustrate the method. The sampled crack paths can be used, in particular, to enrich datasets and perform uncertainty quantification for a fixed (and reasonably small) number of full-scale, high-fidelity simulations. While the approach was applied to synthetic data, it should be noticed that it could also be deployed on experimentally characterized crack profiles.

Declaration of Competing Interests

The authors declare that they have no known competing financial interests or personal relationships that could have appeared to influence the work reported in this paper.

Acknowledgments

References

[1] M.A. Bessa, R. Bostanabad, Z. Liu, A. Hu, D.W. Apley, C. Brinson, W. Chen, W. Liu, A framework for data-driven analysis of materials under uncertainty: Countering the curse of dimensionality, Comput. Methods Appl. Mech. Eng. 320 (2017) 633–667, doi:10.1016/j.cma.2017.03.037.

[2] J. Ling, R. Jones, J. Templeton, Machine learning strategies for systems with invariance properties, J. Comput. Phys. 318 (2016) 22–35.

[3] J. Ghaboussi, J.G. Jr, X. Wu, Knowledge-based modeling of material behavior with neural networks, J. Eng. Mech. 117 (1991) 132–153.

[4] G. Ellis, C. Yao, R. Zhao, D. Penumadu, Stress-strain modeling of sands using artificial neural networks, J. Geotech. Eng. 121 (1995) 429–435.

[5] Y. Shen, K. Chandrashekhara, W. Breig, L. Oliver, Finite element analysis of v-ribbed belts using neural network based hyperelastic material model, Int. J. Non-Linear Mech. 40 (2005) 875–890.

[6] B. Le, J. Yvonnet, Q.-C. He, Computational homogenization of nonlinear elastic materials using neural networks, Int. J. Numer. Methods Eng. 104 (2015) 1061–1084.

[7] T. Furukawa, G. Yagawa, Implicit constitutive modelling for viscoplasticity using neural networks, Int. J. Numer. Methods Eng. 43 (1998) 195–219.

[8] K. Wang, W.C. Sun, A multiscale multi-permeability poroplasticity model linked by recursive homogenizations and deep learning, Comput. Methods Appl. Mech. Eng. 334 (2018) 337–380.

[9] D. Ozturk, S. Kotha, A.L. Pilchak, S. Ghosh, Parametrically homogenized constitutive models (phcms) for multi-scale predictions of fatigue crack nucleation in titanium alloys, J. Minerals Metals Mater. Soc. 71 (2019) 2657–2670.

[10] F.E. Bock, R.C. Aydin, C.J. Cyron, N. Huber, S.R. Kalidindi, B. Klusemann, A review of the application of machine learning and data mining approaches in continuum materials mechanics, Front. Mater. 6 (110) (2019).

[11] A.M. Tartakovsky, C.O. Marrero, D. Tartakovsky, D. Barajas-Solano, Learning parameters and constitutive relationships with physics informed deep neural networks (2018) arXiv:1808.03398.

[12] M. Raissi, P. Perdikaris, G.E. Karniadakis, Machine learning of linear differential equations using gaussian processes, J. Comput. Phys. 348 (2017) 683–693.

[13] M. Raissi, G.E. Karniadakis, Hidden physics models: Machine learning of nonlinear partial differential equations, J. Comput. Phys. 357 (2018) 125–141.

[14] M. Raissi, P. Perdikaris, G.E. Karniadakis, Physics-informed neural networks: A deep learning framework for solving forward and inverse problems involving nonlinear partial differential equations, J. Comput. Phys. 378 (2019) 686–707.

[15] M. Raissi, A. Yazdani, G.E. Karniadakis, Hidden fluid mechanics: A Navier-Stokes informed deep learning framework for assimilating flow visualization data (2018) arXiv:1808.04327.

[16] M. Raissi, Z. Wang, M.S. Triantafyllou, G.E. Karniadakis, Deep learning of vortex-induced vibrations, J. Fluid Mech. 861 (2019) 119–137.

[17] S. Mo, N. Zabaras, X. Shi, J. Wu, Deep autoregressive neural networks for high-dimensional inverse problems in groundwater contaminant source identification, Water Resources Research 55 (5) (2019) 3856–3881.

[18] K. Xu, E. Darve, The neural network approach to inverse problems in differential equations (2019) arXiv:1901.07758.

[19] R. Cang, Y. Xu, S. Chen, Y. Liu, Y. Jiao, M.Y. Ren, Microstructure representation and reconstruction of heterogeneous materials via deep belief network for computational material design, ASME J. Mech. Des. 139 (2017) 071404.

[20] X. Li, Y. Zhang, H. Zhao, C. Burkhart, C. Brinson, W. Chen, A transfer learning approach for microstructure reconstruction and structure-property predictions, Scientif. Rep. 8 (2018) 13461.

[21] Y. Zhu, N. Zabaras, Bayesian deep convolutional encoder-decoder networks for surrogate modeling and uncertainty quantification, J. Comput. Phys. 366 (2018) 415–447.

[22] R.K. Tripathy, I. Bilionis, Deep UQ: Learning deep neural network surrogate models for high dimensional uncertainty quantification, J. Comput. Phys. 375 (2018) 565–588.

[23] D. Zhang, L. Lu, L. Guo, G.E. Karniadakis, Quantifying total uncertainty in physics-informed neural networks for solving forward and inverse stochastic problems, J. Comput. Phys. 397 (2019) 108850.

[24] Y. Yang, P. Perdikaris, Adversarial uncertainty quantification in physics-informed neural networks, J. Comput. Phys. 394 (2019) 136–152.

[25] B.A. Moore, E. Rougier, D. O'Malley, G. Srinivasan, A. Hunter, H. Viswanathan, Predictive modeling of dynamic fracture growth in brittle materials with machine learning, Comput. Mater. Sci. 148 (2018) 46–53, doi:10.1016/j.commatsci.2018.01.056.

[26] A. Hunter, B.A. Moore, M. Mudunuru, V. Chau, R. Tchoua, C. Nyshadham, S. Karra, D. O'Malley, E. Rougier, H. Viswanathan, G. Srinivasan, Reduced-order modeling through machine learning and graph-theoretic approaches for brittle fracture applications, Comput. Mater. Sci. 157 (2019) 87–98, doi:10.1016/j.commatsci.2018.10.036.

[27] M. Schwarzer, B. Rogan, Y. Ruan, Z. Song, D.Y. Lee, A.G. Percus, V.T. Chau, B.A. Moore, E. Rougier, H.S. Viswanathan, G. Srinivasan, Learning to fail: Predicting fracture evolution in brittle material models using recurrent graph convolutional neural networks, Comput. Mater. Sci. 162 (2019) 322–332, doi:10.1016/j.commatsci.2019.02.046.

[28] K. Pierson, A. Rahman, A.D. Spear, Predicting microstructure-sensitive fatigue-crack path in 3d using a machine learning framework, J. Minerals Metals Mater. Soc. 71 (2019) 2680–2694.

[29] R. Swischuk, L. Mainini, B. Peherstorfer, K. Willcox, Projection-based model reduction: Formulations for physics-based machine learning, Comput. Fluids 179 (2019) 704–717.

[30] Y. Zhu, N. Zabaras, P.-S. Koutsourelakis, P. Perdikaris, Physics-constrained deep learning for high-dimensional surrogate modeling and uncertainty quantification without labeled data, J. Comput. Phys. 394 (2019) 56–81.

[31] K. Sobczyk, D.J. Kirkner, Stochastic Modeling of Microstructures, Birkhäuser Basel, 2001.

[32] R.J. Adler, J.E. Taylor, Random Fields and Geometry, Springer-Verlag New York, 2007.

[33] R. Geelen, Y. Liu, T. Hu, M. Tupek, J.E. Dolbow, A phase-field formulation for dynamic cohesive fracture, Comput. Methods Appl. Mech. Eng. 348 (2019) 680–711.

[34] C. Miehe, M. Hofacker, F. Welschinger, A phase field model for rate-independent crack propagation: Robust algorithmic implementation based on operator splits, Comput. Methods Appl. Mech. Eng. 199 (45-48) (2010) 2765–2778.

[35] E. Lorentz, S. Cuvilliez, K. Kazymyrenko, Convergence of a gradient damage model toward a cohesive zone model, Comptes Rendus Mécanique 339 (1) (2011) 20–26.

[36] A. Al-Ostaz, I. Jasiuk, Crack initiation and propagation in materials with randomly distributed holes, Eng. Fracture Mech. 58 (5) (1997) 395–420.

[37] M. Skoge, A. Donev, F.H. Stillinger, S. Torquato, Packing hyperspheres in high-dimensional Euclidean spaces, Phys. Rev. E 74 (2006) 041127, doi:10.1103/PhysRevE.74.041127.

[38] V. Ziaei-Rad, L. Shen, J. Jiang, Y. Shen, Identifying the crack path for the phase field approach to fracture with non-maximum suppression, Comput. Methods Appl. Mech. Eng. 312 (2016) 304–321.

[39] C. Soize, R. Ghanem, Data-driven probability concentration and sampling on manifold, J. Comput. Phys. 321 (2016) 242–258, doi:10.1016/j.jcp.2016.05.044.

[40] R.R. Coifman, S. Lafon, A.B. Lee, M. Maggioni, B. Nadler, F.W. Warner, S.W. Zucker, Geometric diffusions as a tool for harmonic analysis and structure definition of data: Diffusion maps, Proc. Natl. Acad. Sci. 102 (21) (2005) 7426–7431, doi:10.1073/pnas.0500334102.

[41] C. Soize, R. Ghanem, C. Safta, X. Huan, Z. Vane, J. Oefelein, G. Lacaze, H. Najm, Q. Tang, X. Chen, Entropy-based closure for probabilistic learning on manifolds, J. Comput. Phys. 388 (2019) 518–533.

[42] C. Soize, Polynomial chaos expansion of a multimodal random vector, SIAM/ASA J. Uncertainty Quantif. 3 (2015) 34–60.

[43] G.N. Milstein, Y.M. Repin, M.V. Tretyakov, Symplectic integration of hamiltonian systems with additive noise, SIAM J. Numer. Anal. 39 (2002) 2066–2088.

[44] A. Brünger, C.L. Brooks, M. Karplus, Stochastic boundary conditions for molecular dynamics simulations of ST2 water, Chem. Phys. Lett. 105 (5) (1984) 495–500.

[45] S. Kale, M. Ostoja-Starzewski, Representing stochastic damage evolution in disordered media as a jump markov process using the fiber bundle model, Int. J. Damage Mech. 26 (2017) 147–161.

[46] D.-A. Hun, J. Guilleminot, J. Yvonnet, M. Bornert, Stochastic multiscale modeling of crack propagation in random heterogeneous media, Int. J. Numer. Methods Eng. 119 (13) (2019) 1325–1344.

[47] N. Nguyen, J. Yvonnet, J. Réthoré, A.B. Tran, Identification of fracture models based on phase field for crack propagation in heterogeneous lattices in a context of non-separated scales, Comput. Mech. 63 (5) (2019) 1047–1068.